Generating Octave-Bandwidth Soliton Frequency Combs with Compact Low-Power Semiconductor Lasers

Travis C. Briles,[1,2,*] Su-Peng Yu,[1,2] Tara E. Drake,[1,2] Jordan R. Stone,[1,2] and Scott B. Papp[1,2]

[1] *Time and Frequency Division, National Institute for Standards and Technology, Boulder, Colorado 80305, USA*

[2] *Department of Physics, University of Colorado, Boulder, Colorado 80309, USA*

(Received 22 January 2020; revised 3 April 2020; accepted 28 April 2020; published 2 July 2020)

We report a comprehensive study of low-power octave-bandwidth single-soliton microresonator frequency combs in both the 1550-nm and 1064-nm bands. Our experiments utilize fully integrated silicon-nitride Kerr microresonators and we demonstrate direct soliton generation with widely available distributed-Bragg-reflector lasers that provide less than 40 mW of chip-coupled laser power. We report measurements of soliton thermal dynamics and demonstrate how rapid laser-frequency control, consistent with the thermal time scale of a microresonator, facilitates stabilization of octave-bandwidth soliton combs. Moreover, since soliton combs are completely described by the fundamental linear and nonlinear dynamics of the intraresonator field, we demonstrate the close connection between modeling and generation of octave-bandwidth combs. Our experiments advance the development of self-referenced frequency combs with integrated-photonics technology and comb-laser sources with a tens-of-terahertz pulse bandwidth across the near infrared.

DOI: 10.1103/PhysRevApplied.14.014006

I. INTRODUCTION

Dissipative Kerr solitons (DKSs) in optical microresonators [1] have emerged as robust chip-scale low-power-consumption frequency-comb sources [2,3]. Research on DKSs has ranged from fundamental studies of nonlinear-optical dynamics traceable to the Lugiato-Lefever equation (LLE) to a wide variety of applications that benefit from compact light sources. Studies on DKS nonlinear dynamics include breathing oscillations [4,5] and their spontaneous synchronization [6], dark-pulse formation [7], soliton crystallization [8], and exploration of new configurations for soliton generation with pulsed [9] and chirped [10] pump lasers. Some applications of DKSs include direct frequency comb spectroscopy [11], dual-comb spectroscopy [12,13], distance measurements [14,15], and optical telecommunications [16]. Octave-spanning solitons with dual dispersive waves (DWs) [17–19] capable of being self-referenced [20] provide a coherent link between the radio-frequency and optical domains, enabling optical frequency synthesis [19,21] and chip-scale optical atomic clocks [22].

Stoichiometric silicon nitride (Si_3N_4) is a premier photonic material in the near-infrared, due to its high nonlinearity, large transparency window, and compatibility with lithographic fabrication techniques [23]. This latter feature allows for sophisticated group-velocity dispersion designs and integration with other photonic elements. Previous demonstrations of octave-spanning single-soliton frequency combs in Si_3N_4 [17–19] have used high on-chip pump powers to overcome suboptimal conditions of resonator group-velocity dispersion, waveguide-resonator coupling, and low intrinsic quality factor (Q_i) of the resonator. Lately, there have been numerous efforts to generate solitons with low pump power [24,25] to enable direct pumping with chip-scale semiconductor lasers without an additional optical amplifier [26–28]. Despite these impressive photonic-integration developments, the bandwidth of these soliton frequency combs has been limited to less than 10 THz (approximately 6.5% of an octave for solitons pumped at 1550 nm). Moreover, direct generation of octave-spanning soliton combs with a semiconductor laser is a critical step for the future development of integrated-photonics frequency-comb systems but has remained an outstanding challenge.

Here, we demonstrate the generation of octave-spanning soliton frequency combs in both the 1550-nm and 1064-nm wavelength bands, with less than 40 mW of on-chip pump power, as well as direct soliton generation with a compact semiconductor laser in the 1064-nm band. By optimizing the waveguide-resonator coupling in high Q_i and dispersion-engineered resonators with a 1-THz free spectral range, the threshold power for Turing pattern generation is as low as 1.3 ± 0.4 mW. Further, we efficiently convert a fraction of the pump laser power into a 1-THz repetition-frequency soliton frequency comb, which spans

*travis.briles@nist.gov

more than one octave and features dual-dispersive-wave power enhancements to assist f-$2f$ frequency-comb self-referencing. These are the elements that are required to construct a compact frequency-comb system based on integrated photonics.

This paper is organized as follows. Section II describes the resonator dispersion design and the generalized experimental setup, including the diagnostic tools for reliable soliton generation. In Sec. III, we discuss the optimization of the waveguide-resonator coupling rate for Kerr-parametric-oscillation-threshold powers at the 1-mW level. Section IV describes the principles of soliton generation in the limit of laser-detuning control, which is much faster than the resonator's thermal dynamics. In Sec. V, we characterize the bandwidth-power scaling in our devices, including the dependence of dispersive-wave power on pump-resonator detuning. In Sec. VI, we use the principles outlined in Secs. II–V to enable direct diode-laser pumping of octave-bandwidth solitons at on-chip powers of 40 mW.

II. METHODS

Figure 1(a) outlines our experimental setup, which is composed of a continuous-wave (cw) pump laser, a SiN photonic chip, and control and characterization instruments. We utilize the Ligentec [29] silicon-nitride foundry for wafer-scale fabrication of approximately 100 photonic chips, each containing a series of approximately 75 ring resonators and associated access waveguides, with a ring coupling section and inverse taper structures at the chip edges for mode conversion to lensed fiber. The cw laser that we frequency tune onto resonance energizes a soliton pulse train, the repetition frequency of which is derived primarily from the ring resonator free-spectral range. The incorporation of numerous devices on one chip allows us to systematically vary the parameters that influence soliton generation and the frequency-comb spectrum; for example, the ratio of the internal loss rate to the output coupling rate and the group-velocity dispersion (GVD, or simply dispersion).

We design SiN ring resonators to produce octave-bandwidth soliton frequency combs, based on knowledge of the resonator-material GVD [30] and two-dimensional (2D) axisymmetric finite-element simulations of the ring resonance frequencies (using COMSOL MULTIPHYSICS [29]). Since all the devices are fabricated on a single wafer, we target our designs around a silicon-nitride device-layer thickness of 652 nm (780 nm) for 1064-nm (1550-nm) laser pumping and a rectangular cross section. We currently understand that the Ligentec foundry process that we use produces approximately vertical side walls, which simplifies the soliton-comb design. By varying the ring-resonator waveguide width (ring width RW), we adjust the overall GVD profile to continuously change the bandwidth of the soliton comb from only tens of nanometers to more than an octave [19,31]. The dominant effect is modification of the second-order GVD coefficient. However, higher-order dispersion is critical to broaden the comb spectrum through dispersive-wave (DW) generation.

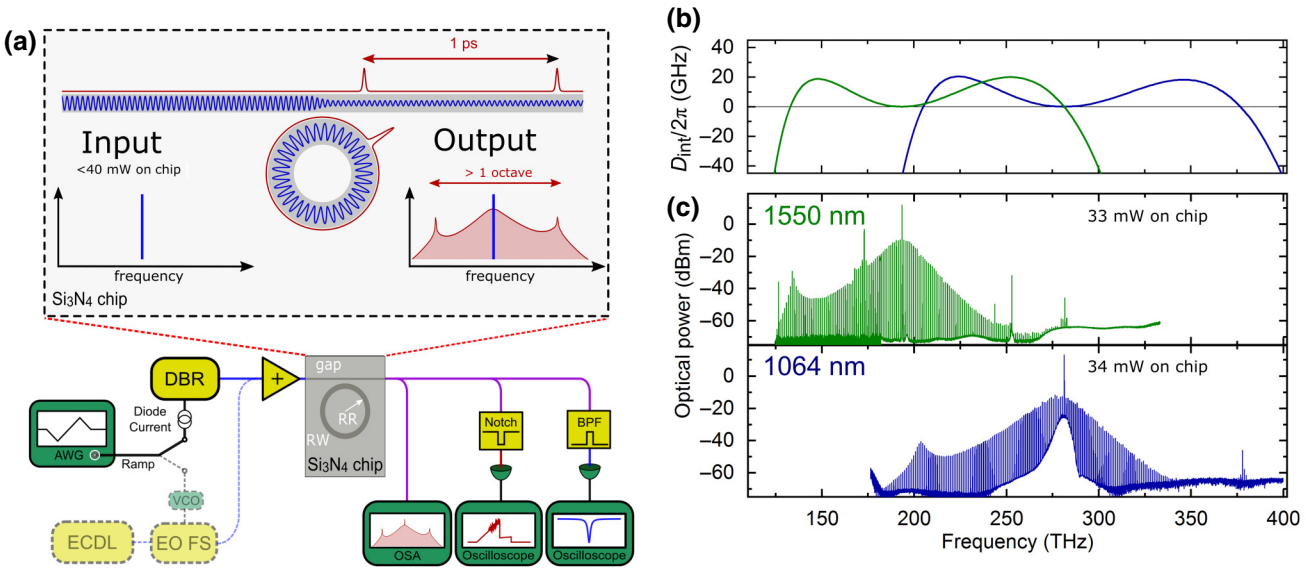

FIG. 1. (a) The experimental setup for soliton generation in optimized Si_3N_4 resonators (bottom) and an enlargement highlighting key processes occurring on chip. AWG, arbitrary waveform generator; ECDL, external-cavity diode laser; EO FS, electro-optic frequency shifter; DBR, distributed-Bragg-reflector laser; OSA, optical spectrum analyzer; BPF, band-pass filter. (b) The dispersion design and (c) the octave-spanning single-soliton spectra obtained at low pump powers at pump wavelengths of 1550 nm (green) and 1064 nm (blue).

The conditions to realize a DW are (1) near-equivalence of a resonator-mode frequency and the corresponding comb mode and (2) the balancing of four-wave mixing gain and resonator loss. The first condition is addressed in Fig. 1(b), which shows a simulation of the integrated GVD ($D_{\rm int}/2\pi$) the zero crossings of which approximate the optical frequency of DWs in the soliton comb spectrum. Here, the parameter RW = 810 nm (RW = 1710 nm) is optimized for 1064-nm- (1550-nm-) wavelength pumping of an octave-bandwidth soliton comb. The utilization of high-resolution lithography to shape soliton frequency combs requires geometry precision at the few-nanometer level, which exceeds current fabrication capabilities. As a result, obtaining a desired resonator dispersion requires fabrication of multiple resonators, which are subsequently screened. This procedure requires a reliable method to generate solitons in any desired resonator.

In this work, we generate solitons with high fidelity by agile control of the pump-laser frequency. We describe two methods, depending on the type of semiconductor laser used—either a tabletop external-cavity diode laser (ECDL) or a compact distributed-Bragg-reflector (DBR) diode laser [see the bottom of Fig. 1(a)]. The pump laser is amplified in either an ytterbium-doped fiber amplifier (1064 nm) or an erbium-doped fiber amplifier (1550 nm). The generic wavelength-dependent optical amplifier is represented in Fig. 1(a) as a yellow triangle with an inscribed plus sign. The amplifier overcomes system losses between the lasers and the on-chip ring resonators, arising primarily from mode conversion between optical fiber and the integrated waveguides. Both methods rely on fast laser-frequency sweeps to mitigate destabilizing thermal transients (for details, see Secs. IV and VI).

In the ECDL-based method [19,31,32], we use a voltage-controlled oscillator (VCO) to drive an electro-optic frequency shifter (EO FS). The VCO sweeps the laser frequency by 5 GHz in a duration of 100 ns. The components and system connections of the EO FS are shown with dashed lines in the lower branch of Fig. 1(a). In the DBR method, the laser frequency is controlled by direct modulation of the injection current of a 1064-nm DBR laser from Photodigm [29] for frequency sweeps of 6.5 GHz in 1.25 μs (Sec. VI provides a complete description). In both methods, the frequency-ramp profiles are generated by an electronic arbitrary-waveform generator (AWG).

We diagnose soliton generation using several techniques. Spectral-domain analysis of stable solitons is performed by diverting a small fraction of the total light coupled off chip to an optical-spectrum analyzer (OSA). For time-domain analysis, we direct the majority of the remaining light to a notch filter centered at the pump wavelength, to isolate the generated comb light from the unconverted pump light. Observation of the photodetected filtered comb power on an oscilloscope during laser sweeps provides a critical diagnostic of soliton formation (see Fig. 3). High-bandwidth electronics (> 150 MHz) allow the boundary between the high-noise modulation-instability (MI) regime at negative (blue) laser detuning and the low-noise soliton regime at positive (red) detuning [1] to be distinguished with high signal-to-noise [see bottom right of Fig. 1(a)].

By use of the EO FS technique and the SiN ring resonators described above, we create the octave-bandwidth soliton combs displayed in Fig. 1(c). The DW wavelengths are in reasonable agreement with the $D_{\rm int}$ approximation. Moreover, the generation of these soliton combs requires 34 mW of on-chip power. The coupling losses at the facets are 3 dB and 6.5 dB for the 1550-nm and 1064-nm devices, respectively. Importantly, DWs offer high power per mode, comparable to that near the center frequency of the comb. However, the realization of this condition requires efficient resonator outcoupling across approximately 200 THz and operation of the pump laser at large red detuning; satisfying these conditions in optimally designed resonators is still a challenge.

III. OPTIMIZING EXTERNAL RESONATOR COUPLING

To achieve the lowest-power soliton microcomb operation, we carefully optimize the external coupling rate of the resonator to the on-chip waveguide. Here, we review the analysis of this problem and we present data to evaluate the results of our optimization. The Lugiato-Lefever equation (LLE) [33,34] provides an accurate model for the soliton behavior in our resonators. In particular, we characterize the pump laser power ($P_{\rm in}$) normalized to the threshold power for parametric oscillation ($P_{\rm th}$) as $F^2 = P_{\rm in}/P_{\rm th}$. The resonator loading is described in terms of the coupling parameter $K = \kappa_c/\kappa_i = Q_i/Q_c$, where κ_i is the intrinsic loss rate of the resonator and κ_c is the coupling rate. It is also important to characterize the pump-laser frequency detuning from the cavity resonance Δ, which we normalize to half the resonator total loss rate $\kappa_{\rm tot} = \kappa_i + \kappa_c$ so that $\Delta = 2\pi\left(\nu_0 - \nu_{\rm p}\right)/\kappa_{\rm tot}/2$. Here, ν_0 and ν_p are the optical frequency of the resonator and pump modes, respectively. The effects of detuning are discussed in more detail in Secs. IV and V. These quantities are related to the associated quality factors Q_c and Q_i by $\kappa_c/2\pi = \nu_0/Q_c$ and $\kappa_i/2\pi = \nu_0/Q_i$, respectively. The threshold power for parametric oscillation [35,36] is

$$P_{\rm th} = \frac{\pi}{8}\frac{n}{n_2}\frac{\nu_0}{\nu_{\rm FSR}}\frac{A_{\rm eff}}{Q_i^2}\times\frac{(1+K)^3}{K}, \tag{1}$$

where n is the refractive index, $n_2 = 2.4\times10^{-19}{\rm m}^2/{\rm W}$ [37] is the nonlinear refractive index, $\nu_{\rm FSR}$ is the resonator free spectral range (FSR), and $A_{\rm eff}\approx 0.5\ \mu{\rm m}^2$ is

the effective mode-area of the resonator. One may optimize the resonator-material selection and other properties to reduce $P_{\rm th}$. Interestingly, Eq. (1) indicates that the absolute minimum threshold occurs for a setting of $K = 0.5$.

Figure 2 presents our experimental data and analysis of threshold power in devices designed for use with a 1064-nm laser. Operationally, we characterize the resonator Q_i and Q_c values with measurements of a device's transmitted $P_{\rm in}$. The minimum transmission on resonance T is related to K by the relation $T = [(1-K)/(1+K)]^2$. In Fig. 2(a), we explore how the external coupling rate $\kappa_c/2\pi$ changes with the geometrical gap size between the resonator and the waveguide. These devices use a straight waveguide coupler with a single point of closest approach to the resonator. (The external coupling rate is also controlled by the geometry of the coupling region.) For these measurements, we use different device samples on the same chip with a programmed variation in the gap size and we perform these measurements at low power (approximately 50 μW) so that thermal bistability and optical nonlinearity are negligible. We measure five devices with nominally identical RWs (0.85 μm), access-waveguide widths (0.51 μm), and film thicknesses (652 nm), but with waveguide-resonator gaps ranging from 420 to 820 nm in 100-nm steps. Moreover, we measure all the resonances in the optical-frequency range from 280 to 294 THz. The error bars correspond to the standard deviation of these measurements. As expected, κ_c decreases nearly exponentially with the gap distance.

With our characterization of K, we present measurements of the resonator transmission $T(K)$ [Fig. 2(b), top] and the parametric oscillation threshold power $P_{\rm th}(K)$ [Fig. 2(b), bottom] alongside the expected theoretical behavior (solid lines). We characterize $P_{\rm th}(K)$ by the in-waveguide pump-laser power required to generate signal and idler sidebands when the laser frequency is tuned to resonance. Here, the measurements are performed over the optical-frequency range 280–284 THz and the error bars indicate one standard deviation. The transmission measurements demonstrate under-, critical- and over-coupling of the resonator, depending on the gap. The measurements of $P_{\rm th}$ demonstrate the most power-efficient parametric oscillation with slight undercoupling, i.e., $\kappa_c = 0.5\kappa_i$. These behaviors match our expectations from Eq. (1), as indicated by the solid-line model predictions in Fig. 2(b), which we obtain based on the measured Q_i and no other free parameters. Indeed, the threshold power for oscillation with these devices is approximately 1 mW.

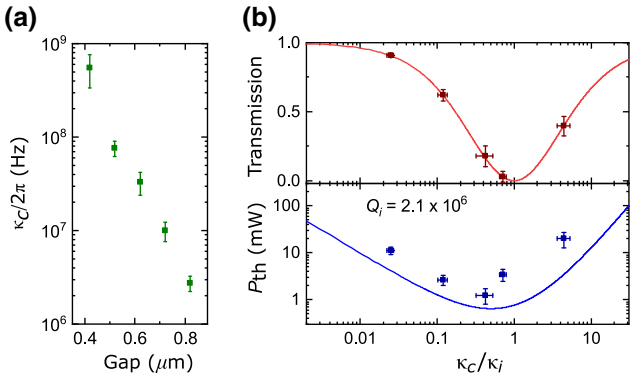

FIG. 2. The optimization of the waveguide-resonator coupling rate $\kappa_c/2\pi$ for a 1064-nm design. (a) The measured $\kappa_c/2\pi$ as a function of the nominal gap distance averaged over measurements from 280 to 294 THz. (b) The measured on-resonance pump (top) and four-wave-mixing threshold power as a function of the coupling parameter κ_c/κ_i over the bandwidth of our optical amplifier (280–284 THz).

IV. SOLITON GENERATION WITH FAST DETUNING CONTROL

The primary benefit of the EO FS technique is increased soliton stability resulting from the very high sweep rates that can be obtained. These sweeps are well suited to the unique challenge of fast thermal dynamics in compact SiN resonators [17,38,39] because they enable detuning control at the primary thermal relaxation time scale ($\tau_{\rm th} \approx$ 100–200 ns) of the ring resonator. Hence, an EO FS can be programmed to mitigate thermal instabilities associated with the transition between the MI and soliton regimes. In this section, we give a detailed procedure for using an EO FS to optimize soliton formation. The ideas presented here directly extend to the diode-current-modulation method presented in Sec. VI.

According to the LLE, DKS properties are determined by the resonator nonlinearity, dispersion, and loss, as well as two external parameters; the pump-laser power and the relative pump-resonator detuning [40,41]. Importantly, there is a pump-power-dependent detuning existence range over which the soliton can stably propagate. It is bound on one end by the boundary between the MI regime and soliton regime at $\Delta_{\rm min} \geq \sqrt{3}$. In the absence of higher-order dispersion, the maximum accessible detuning is given by $\Delta_{\rm max} = \pi^2 F^2/8$. Within the soliton existence range, theoretical scaling laws [42] predict that the soliton peak power and bandwidth monotonically increase with detuning [41,43]. We note that the scaling law for soliton power has recently been extended to include Raman effects [44]. Although an analytic estimate for $\Delta_{\rm max}$ is unavailable in the case of strong higher-order dispersion, our numerical simulations of the LLE indicate that $\Delta_{\rm max} = \pi^2 F^2/8$ remains approximately correct.

Here, we are interested in the detuning dynamics caused by programmed laser-frequency sweeps as well as thermal relaxation of the resonator. Accordingly, we modify the expression for the detuning to explicitly include

dependence on temperature T:

$$\Delta(T) = \frac{2\pi\left[\nu_0(T) - \nu_p\right]}{\kappa_{\mathrm{tot}}/2}. \tag{2}$$

The benefit of fast frequency sweeps is best illustrated by studying the soliton thermal dynamics associated with the MI-soliton transition in the limit of slow detuning control. Figure 3(a) shows the final evolution of soliton power as the pump laser (initially blue detuned) is scanned over a range of > 30 GHz at a rate of approximately 500 GHz/s (the first 60 ms of the sweep are not shown). Three consecutive scans are overlaid in different shades of red. Although the data shown in Fig. 3 are obtained with air-clad devices having a SiN thickness of 615 nm and RW = 1788 nm [19], the results apply to oxide-clad resonators as well. The transition from the MI state to the soliton states with $N = 3$, 2, or 1 pulses is accompanied by a precipitous drop in intracavity power, resulting in significant cooling. Consequently, ν_0 rapidly blue shifts toward its "cold-cavity" frequency while the pump-laser frequency changes minimally. Once $\Delta(T)$ exceeds the existence range (i.e., too red, $\Delta > \Delta_{\mathrm{max}}$), the soliton is lost over a duration comparable to the photon lifetime (a few nanoseconds). The duration of the soliton steps in this regime of adiabatic detuning control is a complicated function of the change in intracavity power and temperature [17] as well as the extent of the pump-power-dependent soliton existence range (see Sec. V) but they are generally the same order of magnitude as τ_{th} [17,38,39]. The absence of step durations > 1 μs, even when the scan speed is reduced by over an order of magnitude, indicates that thermal relaxation is the dominant mechanism that determines the step duration in the adiabatic regime.

Figure 3(b) examines the soliton dynamics in the opposite regime, where the pump laser is tuned faster than the thermal dynamics. The pump laser starts blue detuned and its frequency is decreased by 5 GHz in under 100 ns, reaching the effectively red-detuned single-soliton state near the end of the ramp, which occurs at approximately 0 ns. Because the soliton state is accessed so quickly, the resonator is still in approximate thermal equilibrium with the ambient environment immediately after generating the soliton. The sudden increase in intracavity power results in delayed "thermal charging," which red shifts ν_0 and eventually causes the soliton to be lost at small detunings when $\Delta < \Delta_{\mathrm{min}}$ [approximately 14 μs in Fig. 3(b)]. Since the change in intracavity power between the cold-cavity and the single-soliton state is typically smaller than the change between the MI state and the single-soliton state, the corresponding temperature changes are typically smaller for the fast-sweeping method compared to adiabatic sweeps. This often results in longer soliton steps as shown in Fig. 3(b) and is a principal benefit of this method. After loss of the soliton state, the comb traces back over the blue-detuned MI states. A double-exponential fit to the decaying tails on the blue-detuned side gives time constants of $\tau_{\mathrm{th}}^{(1)} \approx 100$ ns and $\tau_{\mathrm{th}}^{(2)} \approx 1.5$ μs. The faster of these is attributed to thermalization of the approximately 0.5 $\mu\mathrm{m}^2$ transverse-mode area and the slower with the thermalization of the resonator as a whole [45]. A third time scale on the order of 100 μs–1 ms is not evident in Fig. 3(b) but it is attributed to

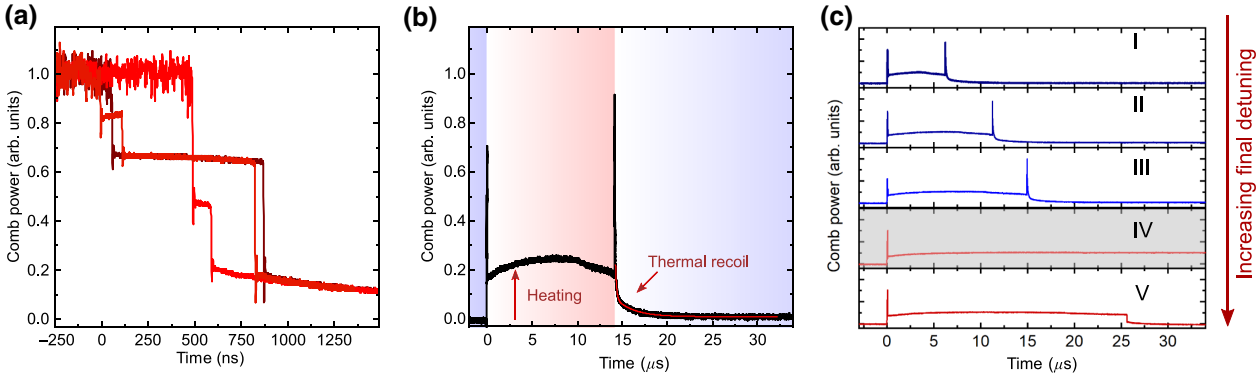

FIG. 3. The soliton thermal dynamics and optimization of fast laser-frequency sweeps with an EO FS pump source. (a) The slow-sweep regime: three consecutive adiabatic sweeps across the cavity resonance, shown in different shades of red. Sweeps in this regime result in cooling and soliton step durations that are limited by the resonator's thermal relaxation rate. The soliton is lost when $\Delta > \Delta_{\mathrm{max}}$ (i.e., too red). (b) The fast-sweep regime: a sweep that accesses the soliton state in a time shorter than τ_{th} results in delayed heating. The soliton state is lost when $\Delta < \Delta_{\mathrm{min}}$ (i.e., too blue). The step durations are typically longer than in the adiabatic case due to the smaller magnitude of ΔT. (c) The optimization of soliton generation with fast sweeps using the principles of (a) and (b). An increase in the final detuning results in an increased step duration for panels I–III, followed by eventual loss of the soliton state at small blue detunings when $\Delta < \Delta_{\mathrm{min}}$, as in (b). A stable soliton state is reached in panel IV. Further increases result in loss of the soliton state at large red detunings, $\Delta > \Delta_{\mathrm{max}}$, as in (a). The red (blue) traces correspond to cases where the final state is effectively red (blue) detuned.

thermalization of the entire chip. The third time scale and its associated temperature changes can be altered somewhat by improving the thermal conductivity between the chip and its mount.

Figure 3(c) outlines how the general behavior illustrated in Figs. 3(a) and 3(b) is used to optimize the laser-frequency ramp for successful generation of solitons. To stabilize the soliton state, the final value of the detuning is progressively increased to chase the thermally red-shifting resonance. Each of the five panels in Fig. 3(c) corresponds to a different final detuning, which increases monotonically from panel I to panel V. In panels I–IV, the increase in final detuning leads to an increased duration of the soliton state until a stable soliton is generated that can circulate indefinitely within the cavity (panel IV). An increase of the detuning past the existence range ($\Delta > \Delta_{max}$) results in the soliton being lost within a few nanoseconds without retracing the blue-detuned MI regime (panel V), similar to the traces in Fig. 3(a).

In samples with large thermo-optic shifts, it may be necessary to include second- and third-order ramps to address the higher-order thermal-relaxation time scales. Since these additional ramps are active while the resonator temperature is relaxing, one must consider the dynamics of both ν_0 and ν_p in Eq. (2). The additional ramps should be optimized using the slope of the detuning-dependent soliton-power oscilloscope trace. Because of the positive correlation between the soliton power and the detuning [41,44], a change in soliton power over time indicates a commensurate change in Δ. In particular, if the soliton power is increasing (decreasing) during the additional ramp segments, this suggests that the applied ramp rate is too fast (slow) compared to the relevant thermal relaxation. The rate should be adjusted until a flat soliton power trace is obtained. The final detunings of these ramps should be adjusted according to the principles outlined in Fig. 3(c).

V. OPTIMIZING THE SOLITON FREQUENCY COMB WITH LASER DETUNING

Following initiation of the soliton frequency comb with either frequency-agile scanning technique, we perform a fine adjustment of the pump-cavity detuning that is designed to increase the soliton-comb bandwidth and, in particular, increase the intensity of both the short-wavelength and long-wavelength dispersive waves (SDW and LDW, respectively), which is important for self-referencing. In this section, we demonstrate the results of this fine adjustment.

In the absence of interference from the phase-dependent cw background and the DWs [46], the DW intensities generally increase monotonically with detuning, reaching the maximum just before the soliton is lost at the edge of the soliton existence range. As a result, for a given pump power, the most intense DWs are found near Δ_{max}. To increase the DW intensity further, larger F^2 values are required to reach correspondingly larger values of Δ_{max}.

Figure 4 investigates how the solitons shown in Fig. 1 change with the pump power and pump-resonator detuning. Here, the EO FS technique is used in both the 1550-nm- and 1064-nm-wavelength bands but the results are general and independent of the soliton generation method. We note that amplified spontaneous emission is not removed with a band-pass filter before the resonator for the 1064-nm spectra (bottom panel). Once solitons are obtained, the laser frequency is decreased to grow the soliton bandwidth, with the broadest spectra occurring near the experimentally determined value of Δ_{max}. All spectra in Fig. 4 are recorded at this condition. Solitons are initially generated with approximately 20 mW of pump power (red traces) and each shows relatively weak LDWs and no measurable SDW. Significant SDWs are not obtained until the pump power is increased by 50% to 33–34 mW (green traces) corresponding to $F^2 = 25$ and 17 for the 1550-nm and 1064-nm cases, respectively. For both cases, the LDW increases by 17 dB and the SDW emerges at −46 dBm. Another 50% increase in the pump power results in smaller increases in the DW intensity. Numerical LLE simulations for the 1064-nm case show a similar dependence of DW intensities on the pump power and detuning. Simulated soliton envelopes near Δ_{max} are shown in the bottom panel of Fig. 4 for each power under consideration. The general behavior reflected in the experimental and simulation results has important practical

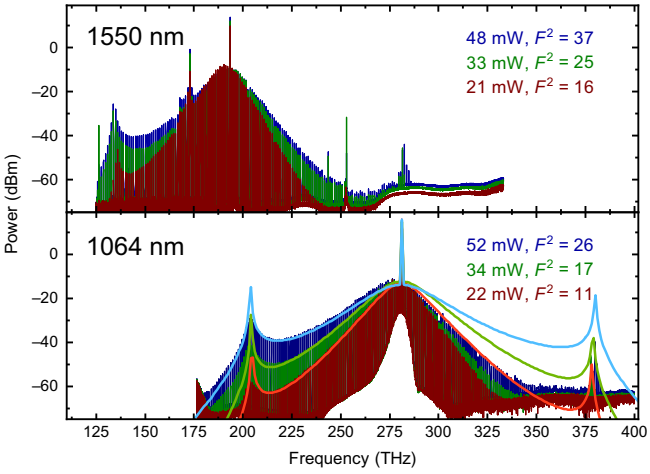

FIG. 4. Soliton spectra for different settings of the pump-laser power and detuning. For each spectrum, the detuning is increased to the corresponding pump-power-dependent value of Δ_{max}. The top (bottom) panel displays data with a 1550-nm (1064-nm) laser. For the 1064-nm data, the spectral envelopes from LLE simulations are shown as solid lines. The large discrepancy in spectral power at high optical frequencies is attributed to poor coupling conversion from the ring resonator to the on-chip coupling waveguide.

consequences for self-referencing applications. Namely, it suggests that much higher pump powers are required to generate significant DWs than are required for simple soliton generation. We also note that the large discrepancy in the absolute SDW power between the experiment and simulation is in agreement with the expected poor performance of straight-waveguide couplers at short wavelengths [47].

VI. DIRECT DIODE-LASER PUMPING OF OCTAVE-BANDWIDTH SOLITON COMBS

Given our detailed understanding of the EO FS technique that enables reliable generation of stable octave-span solitons (Sec. IV), we adapt this approach for use with more compact and integration-ready semiconductor lasers. This offers the potential of a simplified and lower-power-consumption comb system. Figure 5 shows our characterization of diode lasers for this purpose and our observation of octave-span soliton combs.

The primary challenge that arises in adapting the EO FS technique to direct diode-current modulation is duplicating the simultaneously large range and short-duration frequency sweep. Current modulation of diode lasers is complicated by the presence of two distinct mechanisms responsible for changing the laser frequency: (1) carrier density effects and (2) direct Joule heating of the diode junction [48]. At low Fourier frequencies, the modulation response is dominated by thermal effects, where an increase in current heats the diode and leads to a decrease of the laser frequency. Beyond the thermal cutoff frequency f_c, the response is dominated by carrier-density effects, where an increase in diode current leads to an increase of the laser frequency. The value of f_c depends on the geometry and composition of the laser cavity but is typically in the range of 10 kHz to 1 MHz. However, the opposite phase of the thermal and carrier-density tuning coefficients complicates optimization of the ramp waveform for soliton generation. Therefore, we avoid the carrier-density regime altogether. In this case, achieving a high-bandwidth frequency modulation requires a small-volume laser cavity that offers a fast thermal relaxation time.

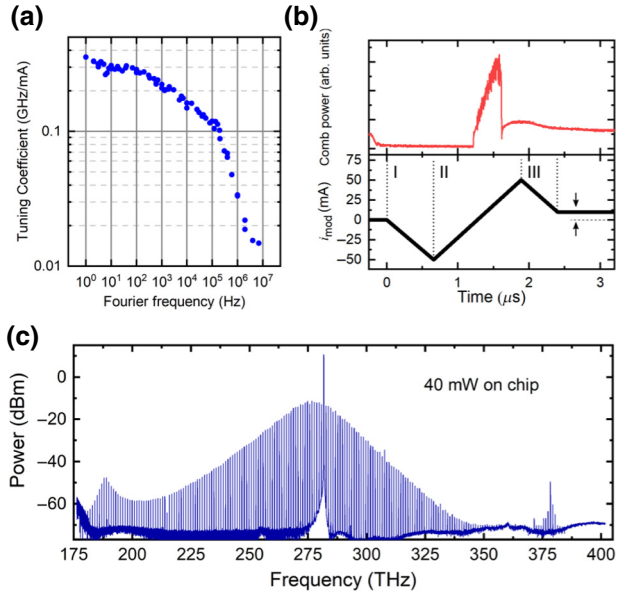

FIG. 5. Soliton generation with direct modulation of the laser-diode current. (a) The measured frequency-modulation response of the DBR laser. (b) The photodetected comb power during soliton generation (top) and the corresponding applied three-segment laser-current ramp (bottom). (c) The spectrum of single soliton obtained with 40 mW of on-chip pump power.

Figure 5(a) shows the measured frequency-modulation response of a short-cavity DBR laser operating at 1064 ± 0.5 nm. The free-space laser output passes through an optical isolator before coupling to fiber. The magnitude response is measured as a function of the Fourier frequency between 10^0 and 10^7 Hz with a calibrated 500-MHz Mach-Zehnder interferometer. The low-frequency tuning coefficient is 0.35 GHz/mA and falls to 0.1 GHz/mA by 100 kHz.

Based on the modulation response of the DBR laser, we design a laser-frequency-ramp sequence for soliton generation using the results of Sec. IV. The optimized ramp profile is an asymmetrical triangle waveform, consisting of three segments [see the bottom panel of Fig. 5(b)]. This modulation current i_{mod} is added to a dc bias current of several hundred milliamperes. Initially, the laser is set to a positive (red) frequency detuning and minimal pump power is coupled to the resonator. In ramp segment I, the current is decreased by 50 mA, which tunes the laser frequency above the cavity resonance (blue detuned). In segment II, the current is increased by 100 mA, decreasing the frequency by 6.5 GHz in 1.25 μs. This ramp segment generates a modulation instability pattern in the resonator that seeds the generation of a single soliton [see the top panel of Fig. 5(b)].

Once the soliton is generated at the end of segment II, we apply a final segment (III) to ensure that the soliton is stable. In contrast to segment II, where the ramp parameters are chosen to minimize thermal transients in the SiN resonator, the parameters of segment III are chosen to minimize thermal transients in the DBR-laser cavity. The finite bandwidth of the current modulation response leads to discrepancies between the applied ramp profile and the actual change in laser frequency for operation at the edge of the modulation bandwidth, as done here. These effects are most important at the end of the ramp sequence, where the ramp's high Fourier-frequency components associated with the transition to a dc level are filtered out, causing the laser frequency to drift after the applied ramp has ended. Because these drifts evolve on

the DBR's natural thermal time scale, which is significantly longer than the τ_{th} value of the SiN resonator, they are incompatible with soliton stabilization. The magnitude of the drift is increased if the final current value is different from the initial value at the start of ramp segment I due to a change in the DBR cavity temperature. We use a final current decrease in segment III to effectively counteract this drift. The optimum magnitude of segment III is a balance of maintaining the soliton existence range and keeping the laser in approximate thermal equilibrium [see the arrows in the bottom panel of Fig. 5(b)]. If the magnitude of the current decrease is too small, the slow uncompensated drift in laser frequency causes the soliton to be lost at positive (red) detunings beyond Δ_{max}. If the current is decreased too far, the range of successful initial laser frequencies and pump powers is impractically small and the soliton will generally transition back to the MI regime at negative (blue) detunings. Note that the reversed ramp direction in segment III is reflected in the local maximum of the soliton power shown in Fig. 5(b) and arises from the detuning dependence of the soliton power. The long-term stability of both the DBR- and ECDL-pumped solitons is essentially indefinite, limited only by environmental drifts.

Figure 5(c) shows the spectrum of a soliton generated in the same resonator device as in the bottom panel of Fig. 4, using the frequency-swept DBR-laser technique. Here, we utilize only 40 mW of on-chip power to generate and stabilize this soliton. Moreover, following stabilization of the soliton, we utilize the technique described in Sec. V to optimize the soliton DWs. With the DBR laser, we increase the temperature of the laser package to reach the condition of highest-intensity DW.

VII. CONCLUSION

We report the generation of octave-bandwidth single-soliton frequency combs in integrated SiN photonic circuits using ultralow pump powers that are compatible with existing chip-scale semiconductor lasers. We minimize the required on-chip laser-power consumption by optimizing the external coupling regime. In addition to the 1550-nm and 1064-nm bands, similar results should be possible for octave-spanning combs pumped in the 1310-nm and 1900-nm bands. Moreover, we describe reliable laser-frequency control techniques to generate soliton combs in an arbitrary SiN ring resonator. This is a key to realizing deterministic control of the soliton-comb spectrum for applications such as $f - 2f$ self-referencing. The matching of the optical mode profile of the chip facets to the DBR laser would allow direct pumping without an optical fiber amplifier. The principles of the soliton-generation technique outlined here should be widely applicable to other tunable narrow-line-width semiconductor lasers [49], including distributed-feedback diode lasers (DFBs) and extended DBR lasers integrated on silicon [50].

ACKNOWLEDGMENTS

We thank Cort Johnson and Christine Wang at Draper Laboratories for loan of the DBR laser used in these experiments and Jizhao Zhang and Pablo Acedo for valuable comments on the manuscript. This project was funded by the Defense Advanced Research Projects Agency (DARPA) Atomic Clock with Enhanced Stability (ACES) and Direct On-Chip Digital Optical Synthesizer (DODOS) programs and the National Institute of Standards and Technology (NIST). This work is a contribution of the U.S. Government and is not subject to copyright.

Note added.—We recently became aware of other work on the direct generation of solitons in SiN microresonators using DFB lasers [51].

[1] Tobias J. Kippenberg, Alexander L. Gaeta, Michal Lipson, and Michael L. Gorodetsky, Dissipative Kerr solitons in optical microresonators, Science **361**, eaan8083 (2018).
[2] John L. Hall, Nobel lecture: Defining and measuring optical frequencies, Rev. Mod. Phys. **78**, 1279 (2006).
[3] Theodor W. Hänsch, Nobel lecture: Passion for precision, Rev. Mod. Phys. **78**, 1297 (2006).
[4] Chengying Bao, Jose A. Jaramillo-Villegas, Yi Xuan, Daniel E. Leaird, Minghao Qi, and Andrew M. Weiner, Observation of Fermi-Pasta-Ulam Recurrence Induced by Breather Solitons in an Optical Microresonator, Phys. Rev. Lett. **117**, 163901 (2016).
[5] Erwan Lucas, Maxim Karpov, H. Guo, M. L. Gorodetsky, and Tobias J. Kippenberg, Breathing dissipative solitons in optical microresonators, Nat. Commun. **8**, 736 (2017).
[6] Daniel C. Cole and Scott B. Papp, Subharmonic Entrainment of Kerr Breather Solitons, Phys. Rev. Lett. **123**, 173904 (2019).
[7] Xiaoxiao Xue, Yi Xuan, Yang Liu, Pei-Hsun Wang, Steven Chen, Jian Wang, Dan E. Leaird, Minghao Qi, and Andrew M. Weiner, Mode-locked dark pulse Kerr combs in normal-dispersion microresonators, Nat. Photonics **9**, 594 (2015).
[8] Daniel C. Cole, Erin S. Lamb, Pascal Del'Haye, Scott A. Diddams, and Scott B. Papp, Soliton crystals in Kerr resonators, Nat. Photonics **11**, 671 (2017).
[9] Ewelina Obrzud, Steve Lecomte, and Tobias Herr, Temporal solitons in microresonators driven by optical pulses, Nat. Photonics **11**, 600 (2017).
[10] Daniel C. Cole, Jordan R. Stone, Miro Erkintalo, Ki Youl Yang, Xu Yi, Kerry J. Vahala, and Scott B. Papp, Kerr-microresonator solitons from a chirped background, Optica **5**, 1304 (2018).
[11] Liron Stern, Jordan R. Stone, Songbai Kang, Daniel C. Cole, Myoung-Gyun Suh, Connor Fredrick, Zachary Newman, Kerry Vahala, John Kitching, Scott A. Diddams, and Scott B. Papp, Direct Kerr-frequency-comb atomic spectroscopy, arXiv:1812.09789s (2018).

[12] Myoung-Gyun Suh, Qi-Fan Yang, Ki Youl Yang, Xu Yi, and Kerry J. Vahala, Microresonator soliton dual-comb spectroscopy, Science **354**, 600 (2016).
[13] Avik Dutt, Chaitanya Joshi, Xingchen Ji, Jaime Cardenas, Yoshitomo Okawachi, Kevin Luke, Alexander L. Gaeta, and Michal Lipson, On-chip dual-comb source for spectroscopy, Sci. Adv. **4**, e1701858 (2018).
[14] Myoung-Gyun Suh and Kerry J. Vahala, Soliton microcomb range measurement, Science **359**, 884 (2018).
[15] P. Trocha, M. Karpov, D. Ganin, M. H. P. Pfeiffer, A. Kordts, S. Wolf, J. Krockenberger, P. Marin-Palomo, C. Weimann, S. Randel, W. Freude, T. J. Kippenberg, and C. Koos, Ultrafast optical ranging using microresonator soliton frequency combs, Science **359**, 887 (2018).
[16] Pablo Marin-Palomo, Juned N. Kemal, Maxim Karpov, Arne Kordts, Joerg Pfeifle, Martin H. P. Pfeiffer, Philipp Trocha, Stefan Wolf, Victor Brasch, Miles H. Anderson, Ralf Rosenberger, Kovendham Vijayan, Wolfgang Freude, Tobias J. Kippenberg, and Christian Koos, Microresonator-based solitons for massively parallel coherent optical communications, Nature **546**, 274 (2017).
[17] Qing Li, Travis C. Briles, Daron A. Westly, Tara E. Drake, Jordan R. Stone, B. Robert Ilic, Scott A. Diddams, Scott B. Papp, and Kartik Srinivasan, Stably accessing octave-spanning microresonator frequency combs in the soliton regime, Optica **4**, 193 (2017).
[18] Martin H. P. Pfeiffer, Clemens Herkommer, Junqiu Liu, Hairun Guo, Maxim Karpov, Erwan Lucas, Michael Zervas, and Tobias J. Kippenberg, Octave-spanning dissipative Kerr soliton frequency combs in Si_3N_4 microresonators, Optica **4**, 684 (2017).
[19] Travis C. Briles, Jordan R. Stone, Tara E. Drake, Daryl T. Spencer, Connor Fredrick, Qing Li, Daron Westly, B. R. Ilic, Kartik Srinivasan, Scott A. Diddams, and Scott B. Papp, Interlocking Kerr-microresonator frequency combs for microwave to optical synthesis, Opt. Lett. **43**, 2933 (2018).
[20] David J. Jones, Scott A. Diddams, Jinendra K. Ranka, Andrew Stentz, Robert S. Windeler, John L. Hall, and Steven T. Cundiff, Carrier-envelope phase control of femtosecond mode-locked lasers and direct optical frequency synthesis, Science **288**, 635 (2000).
[21] Daryl T. Spencer, Tara Drake, Travis C. Briles, Jordan Stone, Laura C. Sinclair, Connor Fredrick, Qing Li, Daron Westly, B. Robert Ilic, Aaron Bluestone, Nicolas Volet, Tin Komljenovic, Lin Chang, Seung Hoon Lee, Dong Yoon Oh, Myoung-Gyun Suh, Ki Youl Yang, Martin H. P. Pfeiffer, Tobias J. Kippenberg, Erik Norberg, Luke Theogarajan, Kerry Vahala, Nathan R. Newbury, Kartik Srinivasan, John E. Bowers, Scott A. Diddams, and Scott B. Papp, An optical-frequency synthesizer using integrated photonics, Nature **557**, 81 (2018).
[22] Zachary L. Newman, Vincent Maurice, Tara Drake, Jordan R. Stone, Travis C. Briles, Daryl T. Spencer, Connor Fredrick, Qing Li, Daron Westly, B. R. Ilic, Boqiang Shen, Myoung-Gyun Suh, Ki Youl Yang, Cort Johnson, David M. S. Johnson, Leo Hollberg, Kerry J. Vahala, Kartik Srinivasan, Scott A. Diddams, John Kitching, Scott B. Papp, and Matthew T. Hummon, Architecture for the photonic integration of an optical atomic clock, Optica **6**, 680 (2019).
[23] David J. Moss, Roberto Morandotti, Alexander L. Gaeta, and Michal Lipson, New CMOS-compatible platforms based on silicon nitride and Hydex for nonlinear optics, Nat. Photonics **7**, 597 (2013).
[24] Xingchen Ji, Felippe A. S. Barbosa, Samantha P. Roberts, Avik Dutt, Jaime Cardenas, Yoshitomo Okawachi, Alex Bryant, Alexander L. Gaeta, and Michal Lipson, Ultra-low-loss on-chip resonators with sub-milliwatt parametric oscillation threshold, Optica **4**, 619 (2017).
[25] Junqiu Liu, Arslan S. Raja, Maxim Karpov, Bahareh Ghadiani, Martin H. P. Pfeiffer, Nils J. Engelsen, Hairun Guo, Michael Zervas, and Tobias J. Kippenberg, Ultralow-power chip-based soliton microcombs for photonic integration, Optica **5**, 1347 (2018).
[26] Brian Stern, Xingchen Ji, Yoshitomo Okawachi, Alexander L. Gaeta, and Michal Lipson, Battery-operated integrated frequency comb generator, Nature **562**, 401 (2018).
[27] N. G. Pavlov, S. Koptyaev, G. V. Lihachev, A. S. Voloshin, A. S. Gorodnitskiy, M. V. Ryabko, S. V. Polonsky, and M. L. Gorodetsky, Narrow-linewidth lasing and soliton Kerr microcombs with ordinary laser diodes, Nat. Photonics **12**, 694 (2018).
[28] Arslan S. Raja, Andrey S. Voloshin, Hairun Guo, Sofya E. Agafonova, Junqiu Liu, Alexander S. Gorodnitskiy, Maxim Karpov, Nikolay G. Pavlov, Erwan Lucas, Ramzil R. Galiev, Artem E. Shitikov, John D. Jost, Michael L. Gorodetsky, and Tobias J. Kippenberg, Electrically pumped photonic integrated soliton microcomb, Nat. Commun. **10**, 680 (2019).
[29] Mention of specific companies or trade names is for scientific communication only and does not constitute an endorsement by NIST.
[30] Kevin Luke, Yoshitomo Okawachi, Michael R. E. Lamont, Alexander L. Gaeta, and Michal Lipson, Broadband mid-infrared frequency comb generation in a Si_3N_4 microresonator, Opt. Lett. **40**, 4823 (2015).
[31] Su-Peng Yu, Travis C. Briles, Gregory T. Moille, Xiyuan Lu, Scott A. Diddams, Kartik Srinivasan, and Scott B. Papp, Tuning Kerr-Soliton Frequency Combs to Atomic Resonances, Phys. Rev. Appl. **11**, 044017 (2019).
[32] Jordan R. Stone, Travis C. Briles, Tara E. Drake, Daryl T. Spencer, David R. Carlson, Scott A. Diddams, and Scott B. Papp, Thermal and Nonlinear Dissipative-Soliton Dynamics in Kerr-Microresonator Frequency Combs, Phys. Rev. Lett. **121**, 063902 (2018).
[33] L. A. Lugiato, F. Prati, M. L. Gorodetsky, and T. J. Kippenberg, From the Lugiato-Lefever equation to microresonator-based soliton Kerr frequency combs, Philos. Trans. R. Soc. A: Math., Phys. Eng. Sci. **376**, 20180113 (2018).
[34] Stéphane Coen, Hamish G. Randle, Thibaut Sylvestre, and Miro Erkintalo, Modeling of octave-spanning Kerr frequency combs using a generalized mean-field Lugiato-Lefever model, Opt. Lett. **38**, 37 (2013).
[35] T. J. Kippenberg, S. M. Spillane, and K. J. Vahala, Kerr-Nonlinearity Optical Parametric Oscillation in an Ultrahigh-Q Toroid Microcavity, Phys. Rev. Lett. **93**, 083904 (2004).
[36] Jiang Li, Hansuek Lee, Tong Chen, and Kerry J. Vahala, Low-Pump-Power, Low-Phase-Noise, and Microwave to

Millimeter-Wave Repetition Rate Operation in Microcombs, Phys. Rev. Lett. **109**, 233901 (2012).

[37] Kazuhiro Ikeda, Robert E. Saperstein, Nikola Alic, and Yeshaiahu Fainman, Thermal and Kerr nonlinear properties of plasma-deposited silicon nitride/silicon dioxide waveguides, Opt. Express **16**, 12987 (2008).

[38] Victor Brasch, Michael Geiselmann, Martin H. P. Pfeiffer, and Tobias J. Kippenberg, Bringing short-lived dissipative Kerr soliton states in microresonators into a steady state, Opt. Express **24**, 29312 (2016).

[39] Amir Arbabi and Lynford L. Goddard, Dynamics of self-heating in microring resonators, Photonics J. IEEE **4**, 1702 (2012).

[40] T. Herr, V. Brasch, J. D. Jost, C. Y. Wang, N. M. Kondratiev, M. L. Gorodetsky, and T. J. Kippenberg, Temporal solitons in optical microresonators, Nat. Photonics **8**, 145 (2014).

[41] Xu Yi, Qi-Fan Yang, Ki Youl Yang, Myoung-Gyun Suh, and Kerry Vahala, Soliton frequency comb at microwave rates in a high-Q silica microresonator, Optica **2**, 1078 (2015).

[42] Stéphane Coen and Miro Erkintalo, Universal scaling laws of Kerr frequency combs, Opt. Lett. **38**, 1790 (2013).

[43] Xu Yi, Qi-Fan Yang, Ki Youl Yang, and Kerry Vahala, Active capture and stabilization of temporal solitons in microresonators, Opt. Lett. **41**, 2037 (2016).

[44] Xinbai Li, Boqiang Shen, Heming Wang, Ki Youl Yang, Xu Yi, Qi-Fan Yang, Zhiping Zhou, and Kerry Vahala, Universal isocontours for dissipative Kerr solitons, Opt. Lett. **43**, 2567 (2018).

[45] V. S. Ilchenko and M. L. Gorodetsky, Thermal nonlinear effects in optical whispering gallery microresonators, Laser Phys. **2**, 1004 (1992).

[46] D. V. Skryabin and Y. V. Kartashov, Self-locking of the frequency comb repetition rate in microring resonators with higher order dispersions, Opt. Express **25**, 27442 (2017).

[47] Gregory Moille, Qing Li, Travis C. Briles, Su-Peng Yu, Tara Drake, Xiyuan Lu, Ashutosh Rao, Daron Westly, Scott B. Papp, and Kartik Srinivasan, Broadband resonator-waveguide coupling for efficient extraction of octave-spanning microcombs, Opt. Lett. **44**, 4737 (2019).

[48] Larry A. Coldren, Scott W. Corzine, and Milan L. Mashanovitch, *Diode Lasers and Photonic Integrated Circuits* (John Wiley & Sons, Hoboken, New Jersey, 2012).

[49] Minh A. Tran, Duanni Huang, and John E. Bowers, Tutorial on narrow linewidth tunable semiconductor lasers using Si/III–V heterogeneous integration, APL Photonics **4**, 111101 (2019).

[50] Duanni Huang, Minh A. Tran, Joel Guo, Jonathan Peters, Tin Komljenovic, Aditya Malik, Paul A. Morton, and John E. Bowers, High-power sub-kHz linewidth lasers fully integrated on silicon, Optica **6**, 745 (2019).

[51] Kenji Nishimoto, Kaoru Minoshima, Takeshi Yasui, and Naoya Kuse, Generation of a microresonator soliton comb pumped by a DFB laser with phase noise measurements, arXiv:2002.00736 (2020).